Growth and characterization of single crystalline NiMnSb thin films and epitaxial NiMnSb/MgO/NiMnSb(001) trilayers

P. Turban, S. Andrieu,* and B. Kierren
Laboratoire de Physique des Matériaux, UMR CNRS 7556, Université Henri Poincaré, Boîte Postale 239, F-54506 Vandœuvre lès Nancy Cedex, France

E. Snoeck
CEMES-CNRS, Boîte Postale 4347, F-31055 Toulouse, France

C. Teodorescu and A. Traverse
LURE, CNRS/CEA/Université Paris Sud, Boîte Postale 34, F-91898 Orsay, France
(Received 5 November 2001; published 19 March 2002)

NiMnSb(001) high-quality epitaxial thin films have been prepared by molecular-beam epitaxy. The growth and morphology of the films have been extensively studied using electron diffraction and scanning tunneling microscopy. We report the presence of various surface structures on the free NiMnSb(001) surface. The structural properties of the prepared single-crystalline NiMnSb films have been analyzed by transmission electron microscopy and x-ray absorption. The typical $C1b$ structure is observed at a large scale with a very good chemical ordering in the unit cell. The magnetic properties have been investigated by x-ray magnetic circular dichroism and a superconducting quantum interferometer device and are compatible with the predicted half-metallic character. These NiMnSb layers have been integrated in single-crystalline NiMnSb/MgO/NiMnSb heterostructures for preparation of magnetic tunnel junctions with half-metallic electrodes.

DOI: 10.1103/PhysRevB.65.134417 PACS number(s): 75.70.−i, 68.55.−a, 73.40.Rw

I. INTRODUCTION

NiMnSb, a semi-Heusler ternary alloy, was, to our best knowledge, the first discovered example of half-metallic ferromagnets.[1] Early band-structure calculations indeed indicate a metallic minority-spin band and an insulating minority-spin band for bulk NiMnSb in the ordered $C1b$ (MgAgAs-type) structure, leading to a 100% spin polarization P of the carriers at the Fermi level.[1–3] Recent developments of spin electronics[4] gave rise to an increased interest in the class of half-metallic materials such as colossal magnetoresistance manganite $La_{0.7}Sr_{0.3}MnO_3$,[5] double perovskite Sr_2FeMoO_6,[6] or transition-metal oxides CrO_2 (Ref. 7) and Fe_3O_4.[8] Due to their total spin polarization, these materials can improve the performance of magnetoresistive devices such as spin valves and magnetic tunnel junctions (MTJ's) or can be used for spin injection in semiconductors. In this context, NiMnSb is of significant interest due to its high magnetic order temperature ($T_c = 730-760$ K).[9–12]

From an experimental point of view, the half-metallic behavior of NiMnSb is well established in the bulk. The magnetic moment is measured by neutron experiments as $4\mu_B$ per primitive unit cell[11–13] in agreement with the expected integer moment for half-metallic ferromagnets. Spin-resolved positron annihilation experiments[14] and infrared reflectance spectroscopy[15] confirmed this half-metallic state. Nevertheless, a small amount of atomic disorder in the unit cell has been shown to destroy the half-metallic behavior in bulk NiMnSb.[16] This strong dependence of NiMnSb electronic properties with structural ordering could be responsible for the relatively low magnetoresistances obtained on NiMnSb-based magnetic tunnel junctions[17,18] or spin valves.[19,20]

Concerning the surface electronic properties, the situation is, however, not so clear. First-principles band-structure calculations predict that NiMnSb surfaces are not half-metallic anymore due to the symmetry breaking at the surface.[21] The NiMnSb surface spin polarization was experimentally measured by various techniques. Results reported in the literature present a quite broad distribution of values. A spin polarization $P = 50\%$ was measured on a polycrystalline NiMnSb surface using spin-polarized photoemission.[22] Superconducting point-contact spectroscopy measurements confirmed a P value of 50%–58%.[23] Spin-polarized tunneling in planar tunnel junctions with an epitaxial NiMnSb layer and a second ferromagnetic or superconducting electrode showed only low P values of 25% and 28%, respectively.[18] On the contrary, Ristoiu *et al.*[24] performed spin-polarized inverse photoemission on epitaxial NiMnSb(001) thin films and measured a spin polarization at the Fermi level for normal incidence very close to 100% above the background. This observed discrepancy between different groups and techniques may be explained by taking into account the high sensitivity of NiMnSb surfaces to classical surface preparation methods.[24,25] The preparation of reproducible bulk-terminated NiMnSb surfaces is thus a fastidious task due to the difficulty in testing the surface chemical ordering.

Despite the crucial importance of preparing well-characterized NiMnSb thin films that present a very high bulk and surface crystalline quality, to our best knowledge, very few experimental works have been devoted to the study of NiMnSb epitaxial growth.[26,27] In this paper we present a detailed study of the growth, and structural and magnetic properties of single-crystalline (001)NiMnSb thin films prepared by molecular-beam epitaxy (MBE). These high-quality NiMnSb thin films were integrated in fully epitaxial

NiMnSb/MgO/NiMnSb(001) hetero structures for the preparation of magnetic tunnel junctions with half-metallic electrodes.

The paper is organized as follows. Experimental details are presented in Sec. II. The growth study of single NiMnSb thin films is presented in Sec. III. The structural and magnetic properties of these films are analyzed in Sec. IV. Finally, Sec. V is devoted to the preparation and characterization of the NiMnSb/MgO/NiMnSb(001) epitaxial trilayer.

II. EXPERIMENTAL DETAILS

The samples were prepared by MBE in a UHV chamber at a residual pressure of 3.10^{-11} h Pa, when the cryopanels were full with liquid nitrogen. Single crystals of (001)MgO were used as substrate after being *ex situ* degreased and *in situ* outgassed up to 1200 K during 1 h. These substrates were indium-sticked to the sample holder to allow an improved thermal contact. Despite the low mismatch between NiMnSb and MgO, NiMnSb thin films directly grown on MgO substrates were polycrystalline as previously observed by Schlomka *et al.*[28] Thus, a (001)V seed layer with thickness in the range 0.5–5 nm was first grown at 400 K on the MgO substrate to promote NiMnSb epitaxial growth. The three alloy components Ni, Mn, and Sb were evaporated from pure materials (99.99% purity for Ni and Mn, 99.999% for Sb) by using Knudsen cells. V seed layers and MgO insulating barriers[29–31] were evaporated by electron bombardment. The chemical purity of all deposits was controlled by Auger electron spectroscopy (AES). A small amount of oxygen contamination was often observed on the V seed layers,[32] but no oxygen or carbon contaminations were detected on NiMnSb surfaces, in the limit of our apparatus sensitivity. Prior to the deposition, Ni, Mn, and Sb cell fluxes were carefully monitored by a quartz-crystal microbalance located in the sample position. We systematically worked with an excess Sb flux and a substrate temperature higher than the Sb desorption temperature (typically 500 K). Thus, Sb flux was not a critical parameter since all exceeding Sb atoms desorbed from the sample surface. The alloy's typical growth rate during deposition was 1 nm/min. During growth the sample holder was rotated to avoid inhomogeneous deposition. The growth was followed in real time by reflection high-energy electron diffraction (RHEED). This technique allowed us to obtain (i) the surface structure, and (ii) the growth mode by recording the 00 streak intensity variation with time.[33] The observation of RHEED intensity oscillations was characteristic of a layer-by-layer growth mode (Frank-Van der Merwe growth).[34] The RHEED patterns also allowed us to obtain qualitative information about the surface roughness. The surface morphology was also investigated by scanning tunneling microscopy (STM) measurements performed at room temperature by using an Omicron STM1 apparatus operating in the constant current mode. W tips were used and prepared by ac electropolishing in a 1 N NaOH solution followed by heating in UHV using electron bombardment. The STM images were not corrected from the drift. Consequently, the real (001)NiMnSb square lattice appeared to be distorted on the STM images.

The samples' structural properties were studied *ex situ* by using high-resolution transmission electron microscopy (HRTEM) in cross-section on cross sectional samples using a 300 keV apparatus whose point resolution is 0.19 nm. The lattice fringes were calibrated using the (002) spacing of the MgO substrate. HRTEM experiments allowed us to study the long-range crystalline quality of the different layers and interfaces. The local chemical ordering in the NiMnSb unit cell was studied by extended x-ray-absorption fine structure (EXAFS). The EXAFS data collection was carried out at 77 K on the D42 station of the DCI ring at LURE at the Ni and Mn *K* edges (8333 and 6539 eV, respectively), and at the Sb L_I edge (4689 eV), with in- and out-of-plane polarization. The total electron yield technique was used. After background removal, the EXAFS oscillations were extracted and normalized to the height of the absorption step edge. The resulting oscillations were characteristic of both the chemical and structural environments of the absorbing atom and are thus fingerprints of the local ordering in the NiMnSb unit cell. For a quantitative analysis, we have calculated the Fourier transform (FT) of the EXAFS spectra, usually called the radial distribution function. The first peak of the FT was the contribution of the first-nearest-neighbors shell, which was analyzed with single-scattering formalism. The contribution of the nearest-neighbors shell to the EXAFS spectra was extracted by calculating the inverse Fourier transform (FT) of the first peak of the FT. This contribution was thus fitted using the classical EXAFS formula[35] with tabulated phase shifts and atomic backscattering amplitudes. We also used a multiple-scattering approach to simulate directly the total EXAFS spectra. For this purpose, we used the FEFF code.[36] With this method, we simply compared for each absorption edge the experimental EXAFS spectra to the calculated one, assuming a perfect NiMnSb structure. One should thus notice that the only two free parameters in the FEFF simulations were the NiMnSb lattice spacing and the Debye temperature. The macroscopic magnetic behavior was studied by using a classical superconducting quantum interferometer device (SQUID) for an in-plane field up to 70 kOe and in the temperature range 4–400 K. The measured magnetization was corrected from the paramagnetic contribution of the MgO substrate. The magnetic properties of each atomic species were also determined by using x-ray magnetic circular dichroism (XMCD) on the Super-Aco ring at LURE. These experiments were performed on two kinds of samples: (i) NiMnSb thin films grown *in situ* in the MBE chamber connected to the synchrotron beamline, and (ii) NiMnSb thin films grown in home MBE capped with a thin MgO layer and transferred at LURE under a box in nitrogen atmosphere. The XMCD experiments were performed at the $L_{2,3}$ absorption edges of Ni and Mn, with the magnetic field aligned with the photon beam. The angle between the x-ray beam and the sample surface was varied from 0° to 90°. The XMCD spectra were collected in the temperature range 10–300 K, by switching the direction of the applied magnetic field and measuring the total electron yield for each photon energy. The degree of polarization of the incoming photons was 52%, and the applied magnetic field was varied in the range 0–1 T. The dichroism signals were calculated by sub-

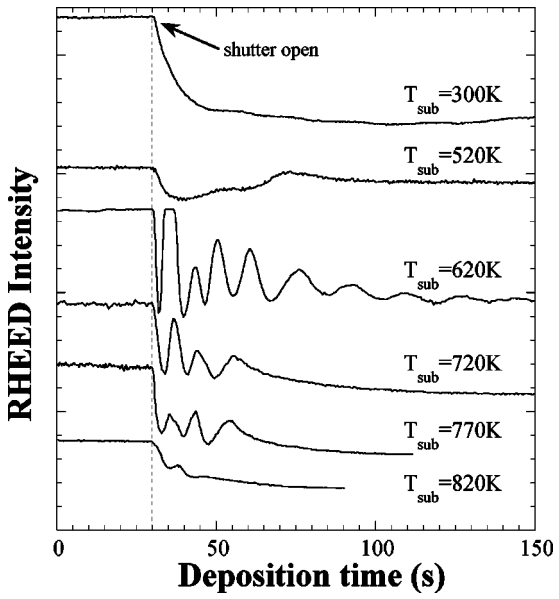

FIG. 1. Evolution of the RHEED intensity of the (00) diffraction rod during epitaxial growth of NiMnSb(001) on a V(001) buffer layer for various substrate temperatures. An arrow marks the beginning of the deposition. The experiments are performed in the first anti-Bragg geometry.

tracting the absorption spectra obtained with positive and negative magnetic fields. The resulting dichroic signal was normalized to the intensity at the L_3 edge calculated after background removal (same method as in Ref. 37), but was not corrected for the incomplete polarization of the incident beam.

III. NiMnSb (001) THIN-FILMS GROWTH STUDY

The surface lattice of MgO(001) is a square with a (100) lattice spacing equal to 0.421 nm. RHEED patterns showed that the V buffer layer grows epitaxially in its (001) planes with the (001)V$\|$(001)MgO and [100]V$\|$[110]MgO. We have investigated by RHEED the growth of NiMnSb on the vanadium buffer layer for a large range of substrate temperatures. NiMnSb epitaxial growth was observed even at room temperature on the (001)V buffer layer. The epitaxial relation between NiMnSb and V films deduced from the RHEED pattern was (001)NiMnSb$\|$(001)V and [100]NiMnSb$\|$[100]V. Thus, one NiMnSb unit cell (lattice spacing $a_{\mathrm{NiMnSb}}=0.591$ nm) was deposited on four V unit cells (lattice spacing $a_{\mathrm{V}}=0.303$ nm). The corresponding low mismatch (-1.7%) allowed us to prepare NiMnSb epitaxial thin films with a low density of structural defects.

During the first stages of epitaxial growth, RHEED oscillations were observed (Fig. 1) which show that the NiMnSb growth on (001)V is two dimensional (2D). A damping of the RHEED intensity oscillations was observed and was presumed to come from the occurrence of a three-dimensional (3D) growth regime, as evidenced by the observed spotty diffraction rods on the RHEED pattern. NiMnSb was thus growing in a Stransky-Krastanov growth mode on the (001)V buffer layer. The number of RHEED intensity oscillations (that is, the extension of the 2D regime) was strongly dependent on the substrate temperature as shown in Fig. 1. For an optimized substrate temperature of 620 K, the layer-by-layer growth was promoted up to 10 monolayers. At this growth temperature, a continuous wetting layer was thus formed and allowed the preparation of NiMnSb thin films with a suitable morphology as discussed hereafter. For a large deposited thickness, and even at 620 K, the NiMnSb film surface roughness increased dramatically and the RHEED patterns presented bright intensity spots typical of bulk diffraction through the 3D growing islands at the surface (Fig. 2).

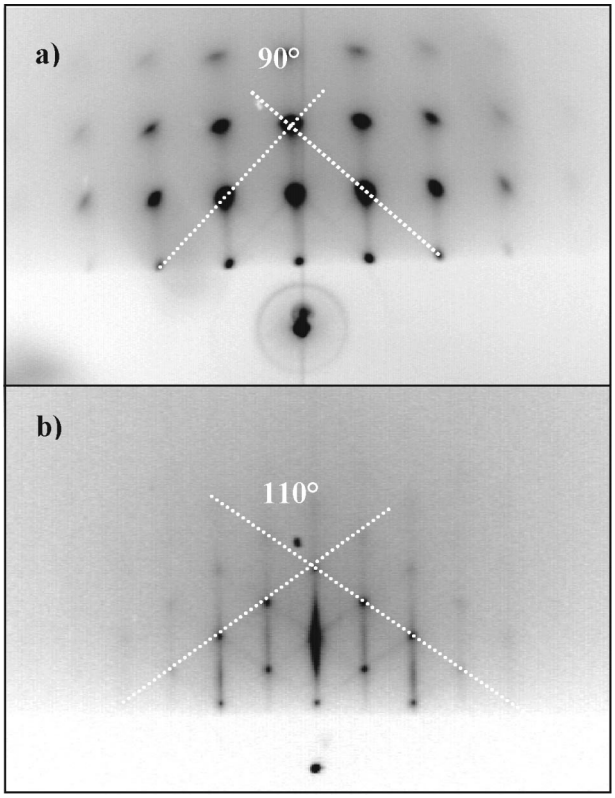

FIG. 2. RHEED patterns observed in the [100] (a) and [110] (b) azimuths of a 70 nm thick NiMnSb(001) film grown at 620 K. Oblique diffraction streaks are clearly visible in both azimuths and correspond to (011) and $(\bar{1}11)$ facets. The white dotted lines are guides for the eye.

Oblique diffraction streaks joining diffraction rods could also be observed on both RHEED patterns along the [110] and [100] azimuths. These chevrons are characteristic of the presence of well-developed facets which are perpendicular to the observed oblique streaks.[38] The observed off-normal streaks were directed at an angle of 45° (respectively, 55°) from the [001] direction when the incident electron beam was aligned with the [100] (respectively, [110]) azimuth and corresponded to (011) [respectively, $(\bar{1}11)$] facets [Figs. 2(a) and 2(b)]. The 3D growing islands were thus made of well-defined truncated polyhedrons with (011)- and $(\bar{1}11)$-type bounding planes. To restore thin 2D diffraction streaks on the RHEED screen, a consequent annealing during growth was necessary to allow the coalescence of the 3D islands. The

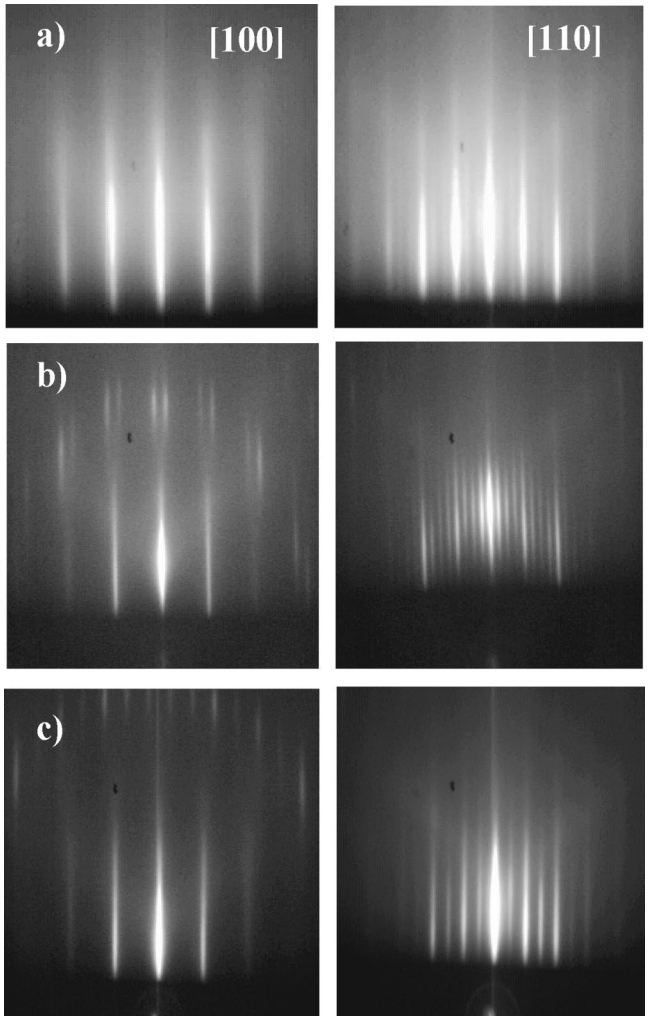

FIG. 3. RHEED patterns obtained in the [100] (left column) and [110] (right column) azimuths of a 70 nm thick NiMnSb(001) layer presenting (a) a (3×1) surface structure after annealing at 730 K; (b) a (4×1) surface structure after annealing at 900 K; and (c) a (2×1) surface structure after annealing at 1000 K.

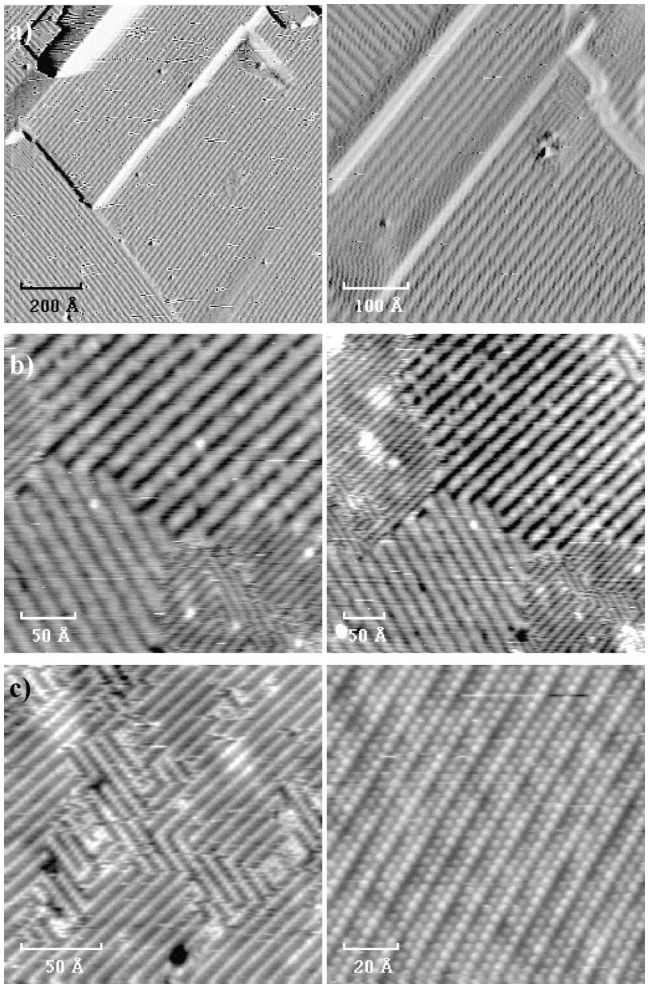

FIG. 4. STM images obtained on NiMnSb(001) surfaces: (a) annealed at 900 K and (4×1) reconstructed, (b) annealed at an intermediate temperature (950 K); (2×1) and (4×1) reconstructed areas are simultaneously observed, and (c) annealed above 1000 K and (2×1) reconstructed.

smoothing of the surface was observed at a substrate temperature around 900 K. It should be noticed that this smoothing was only observed when the impinging Mn, Ni, and Sb fluxes were maintained during the process. Starting the growth directly at 900 K led to 3D islands without any observed smoothing. A 900 K annealing on a 600 K grown film without impinging fluxes also led to rough and faceted surfaces.

Depending on the annealing temperature, various surface structures were observed on the (001)NiMnSb surface after cooling the sample to room temperature (Fig. 3). When the sample was annealed in the range 700–750 K, a (3×1) was observed on the RHEED pattern as shown in Fig. 3(a). Subsequent higher annealing led to the formation of a (4×1) surface structure stable in the range 750–900 K [Fig. 3(a)]. Finally, a (2×1) was observed near 950 K Fig. 3(c)]. Above this temperature, a degradation of the surface morphology and a surface-roughness increase was observed. No clear chemical changing between these various surfaces has been evidenced by AES. In particular, no clear and systematic surface segregation of one of the alloy components has been detected by looking at high-energy Auger peaks (above 400 eV). STM experiments performed on (4×1) reconstructed samples showed smooth surfaces with large atomic terraces (typically 200×200 nm^2) and a typical root-mean-square roughness of 2 nm on 1×1 μm^2 STM images. However, this rms roughness dramatically increased up to 7 nm on the (2×1) reconstructed surface obtained after annealing above 900 K. This is the consequence of the bad wetting of NiMnSb on MgO, which leads to islanding and the appearance of facets as observed by RHEED. On the flat atomic terraces, parallel lines were revealed, expanding in both the [100] and [010] directions (Fig. 4). These lines were regularly spaced from four (respectively, two) atomic distances for the (4×1) [respectively, (2×1)] reconstructed surfaces [Figs. 4(a) and 4(c)]. The surface reconstructions were thus made of two (4×1) and (1×4) [(2×1) and (1×2)] reconstructed domains, turned from each other by 90° and randomly distributed on the sample surface. The atomic resolu-

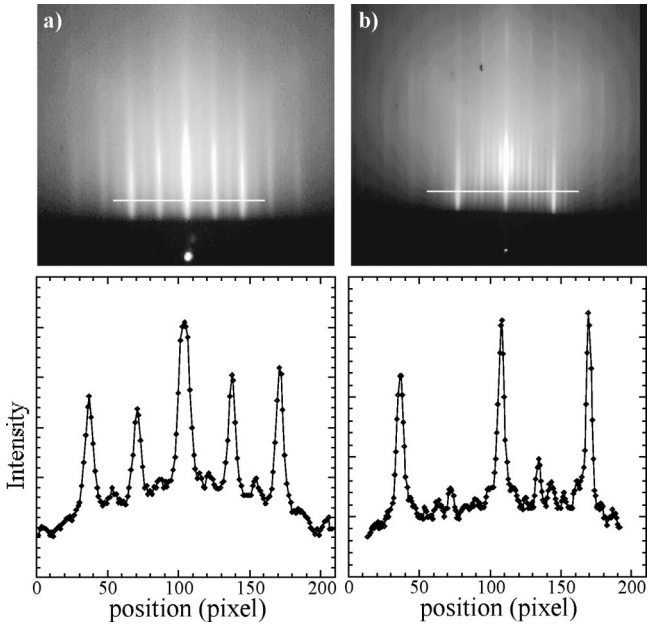

FIG. 5. Evolution of the relative RHEED intensity of the (01) and $(0\bar{1})$ diffraction streaks in the [110] azimuth of a NiMnSb(001) surface annealed (a) at 650 K (left column) and (b) at 900 K (right column).

tion has been obtained on the (2×1) reconstructed surfaces [Fig. 4(b)]. The observed parallel well-defined lines were made of atomic chains which appeared as protrusions on the STM images. One should notice that the transition between the (4×1) and (2×1) surface structures is progressive since for intermediate annealing temperatures (900 K), (4×1) and (2×1) reconstructed domains could be observed simultaneously on the surface as shown in Fig. 4(b).

Finally, during the end of growth annealing, an interesting evolution of the relative intensity between the (01) and (02) diffraction streaks in the [110] azimuth was also observed (Fig. 5). At low temperature, the (01) and (02) rod intensities were very similar, as evidenced by an intensity profile analysis [Fig. 5(a)]. Around 900 K the intensity of the (01) diffraction streaks significantly decreased compared to the (02) one [Fig. 5(b)] in good agreement with the calculated surface structure factor of a well-ordered NiMnSb surface. From these observations, the chemical ordering of the NiMnSb(001) surface was deduced to appear around 900 K. This behavior is a good test to control the effect of the annealing on the chemical ordering.

IV. STRUCTURAL AND MAGNETIC PROPERTIES OF EPITAXIAL NiMnSb (001) THIN FILMS

A. Structural properties

As discussed in the Introduction, the crystalline quality of the NiMnSb thin films seems to be crucial for improving the transport properties. We have thus carefully investigated the structural properties of our epitaxial NiMnSb thin films prepared by MBE. First of all, the influence of growth temperature on the long-range order and the crystalline quality was investigated by HRTEM. Samples prepared at low temperature presented a poor crystalline quality. For example, samples grown at room temperature presented large faulted regions with stacking faults parallel to (111) planes and twins, probably due to the presence of MnSb inclusions in the NiMnSb layer as proposed by Wojcik *et al.*[39] The quality of the NiMnSb films is greatly improved by annealing the films above 850 K at the end of the growth. Figure 6 presents a HRTEM micrograph obtained on such a 100 nm thick (001)NiMnSb film grown at 850 K on a thick (001)V buffer layer. The two different crystalline layers can easily be distinguished in Fig. 6. The Heusler alloy is studied along the $[1\bar{1}0]$ zone axis revealing the (002)- and (111)-type planes.

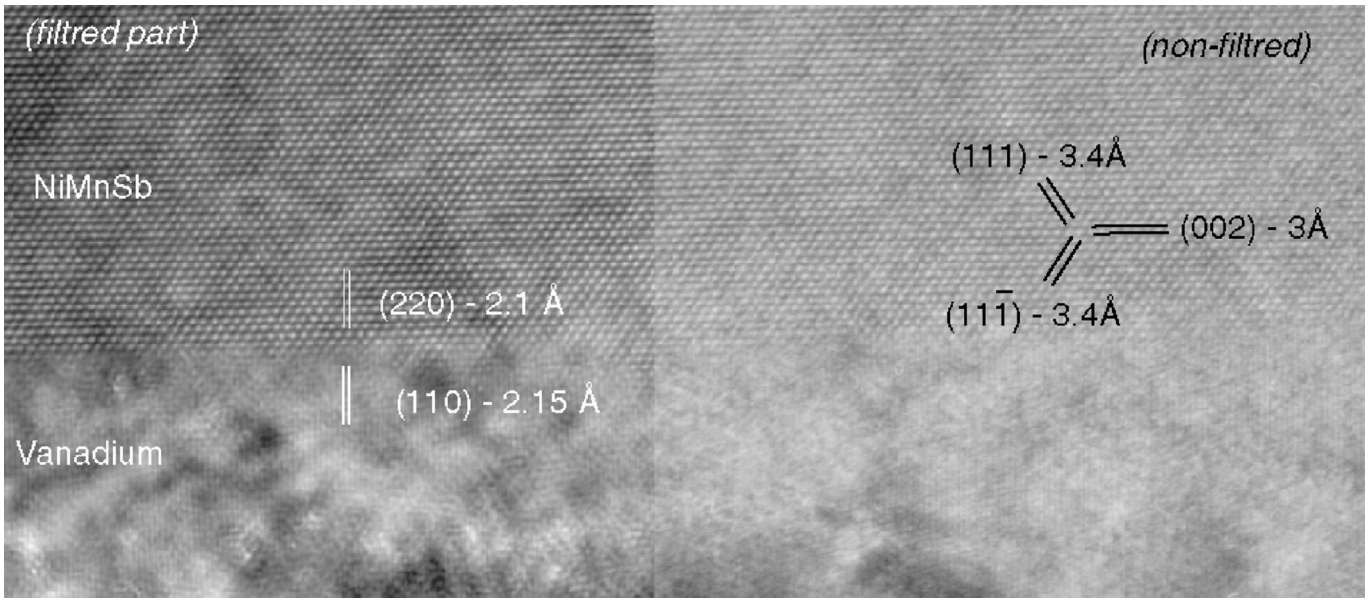

FIG. 6. High-resolution transmission electron micrography of a 100 nm thick NiMnSb(001) layer grown on a V(001) buffer layer and annealed at 850 K.

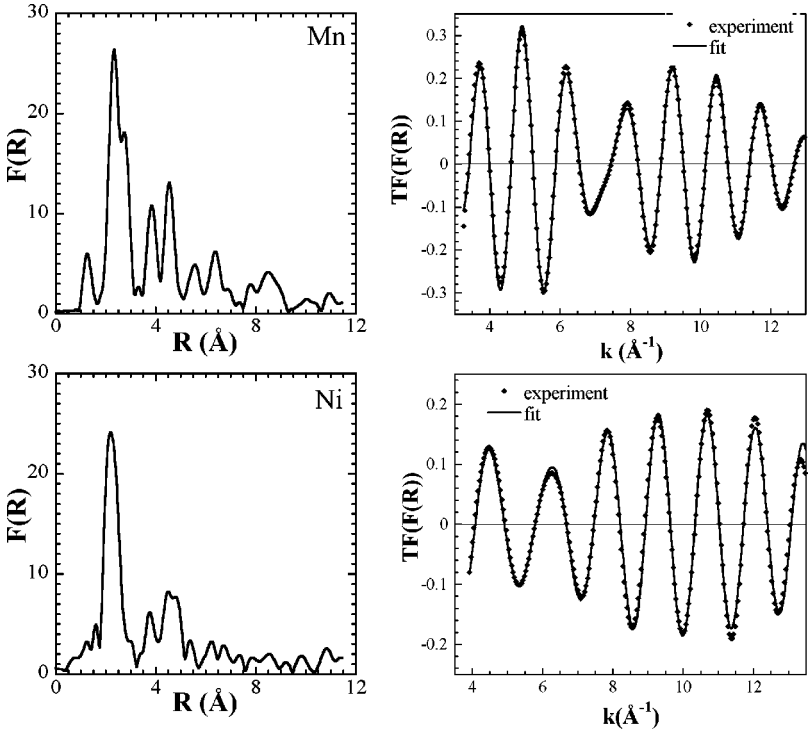

FIG. 7. Contribution of the first-neighbors shell to the experimental EXAFS oscillations recorded at the *K* absorption edges of Mn (top) and Ni (bottom) of a thick NiMnSb sample prepared in the optimized conditions (growth at 650 K and annealing at 900 K) and corresponding fits using the EXAFS formula. The adjustment parameters are given in Table I.

On this HRTEM micrograph, the (220) NiMnSb planes are parallel to the (110) V ones. The epitaxial relationship NiMnSb(100)[220]$\|$V(200)[110] is thus confirmed. The NiMnSb/V interface was very well defined and presented local roughness of less than one nanometer. Concerning the Heusler layer crystalline quality, no defect could be detected at this growth temperature. In particular, no misfit dislocation has been detected at this scale of observation, in good agreement with the low mismatch of the NiMnSb/V system. The obtained diffraction patterns are typical of a MgAgAs-like structure, with a lattice spacing of 0.591 nm, as in the bulk material. To conclude, NiMnSb films grown at a substrate temperature larger than 850 K present a high-quality long-range order.

However, the absence of structural defects is not sufficient to guarantee the electronic properties of the material. A few percent of chemical disorder between the three atomic species in the NiMnSb unit cell is indeed expected to destroy the complete spin polarization.[16] We have thus investigated by EXAFS the local ordering in the NiMnSb unit cell. The best results were obtained for NiMnSb films prepared in the optimized growth conditions reported in Sec. III (growth at 650 K and an end of growth annealing at 900 K). The obtained 100 nm thick NiMnSb layers were coated by a 10 nm (001)V protective layer to avoid oxidization. The EXAFS spectra recorded with a polarization of the incident photons in the sample plane were identical to those recorded with the polarization perpendicular to the plane. Thus the NiMnSb unit cell in the studied films was deduced to be isotropic (no distortion due to epitaxial strain) and the film fully relaxed, which is not surprising according to the large thickness of the films and the low mismatch of the system. We have recorded the EXAFS oscillations at the *K* absorption edges of Ni and Mn, and at the L_1 absorption edge of Sb. The contribution of the first neighbors of the absorbing atom to the total EXAFS signal was extracted by calculating the IFT of the first shell peak in the radial distribution function and simulated using the classical EXAFS formula[35] (Fig. 7).

This method has not been applied to the Sb L_1 edge, due to the poor quality of the data coming from a technical limitation of the beamline for this energy. Another limitation is due to the superimposed oscillations coming from the L_2 EXAFS signal. In Fig. 7 are plotted the radial distribution functions $F(R)$ for Mn and Ni obtained from the Mn and Ni *K* edges, and the corresponding Fourier transform of the first peak of $F(R)$. Assuming a perfect NiMnSb structure with a lattice spacing of 0.591 nm, Ni atoms have four Mn first neighbors and four Sb first neighbors at a distance of 0.256 nm. Mn atoms have four Ni atoms as first neighbors at 0.256 nm, and six Sb atoms as second neighbors at 0.295 nm. These two close coordination shells are thus usually mixed in a single peak in the radial distribution function, and the two types of neighbors have to be taken into account in the EXAFS oscillations simulation. However, it should be noted that in the first peak of the Mn radial distribution function $F(R)$, the contributions coming from the two kinds of neighbors are clearly separated. Both experimental data and simulations of the contribution of the close neighbors to the total EXAFS oscillations recorded at the *K* edges of Ni and Mn are reported in Fig. 7. The fitting parameters were the coordination numbers N_{Ni}, N_{Mn}, and N_{Sb}, the various shell distances $R_{\mathrm{Ni\text{-}Mn}}$, $R_{\mathrm{Ni\text{-}Sb}}$, $R_{\mathrm{Mn\text{-}Ni}}$, and $R_{\mathrm{Mn\text{-}Sb}}$, and the Debye-Waller factors. The values of the best-fitting parameters are reported in Table I. For both absorption edges, the matching between experimental and simulated oscillations was excellent on a large scale of wave-vector values *k*. The obtained coordination numbers as well as the bond lengths were in

TABLE I. Number of nearest neighbors and distance between nearest neighbors obtained by fitting the EXAFS first peak contribution (see text) at the Mn and Ni *K* edges, respectively, and comparison with theoretical values for a perfect $C1b$ structure.

Mn *K* edge	N_{Ni}	R_{Ni} (nm)	σ_{Ni}	N_{Sb}	R_{Sb} (nm)	σ_{Sb}
Experiments	3.5 ± 0.5	0.259 ± 0.020	0.05	6.4 ± 0.5	0.297 ± 0.024	0.07
Theory	4	0.256		6	0.295	

Ni *K* edge	N_{Mn}	R_{Mn} (nm)	σ_{Mn}	N_{Sb}	R_{Sb} (nm)	σ_{Sb}
Experiments	4.2 ± 0.5	0.255 ± 0.015	0.01	3.7 ± 0.4	0.256 ± 0.025	0.04
Theory	4	0.256		4	0.256	

very good agreement with the ones expected for a well-ordered NiMnSb unit cell. The Debye-Waller coefficients are small, confirming the very low degree of static disorder. One should notice that this single-scattering EXAFS analysis at the *K* edges of Ni and Mn was a very efficient method to study the interchange or substitution disorder between the light and heavy atomic species in the unit cell. Due to the very different phase shifts and atomic backscattering amplitudes between the light atoms (Ni and Mn) and the heavy one (Sb) in the material, the contribution of the first coordination shell to the EXAFS oscillations was indeed observed to be very sensitive to any exchange or substitution between light and heavy atoms. Similar experiments on NiMnSb films grown at low temperature evidenced a noticeably higher degree of disorder in the unit cell.

We have also used a more complete data analysis of the EXAFS signal by using a multiple-scattering approach. For this purpose, the complete EXAFS spectra was simulated by using the FEFF7 code, taking into account multiple-scattering paths including up to five successive scattering processes of the photoelectrons. Figure 8 displays both experimental and simulated total EXAFS signals at the three absorption edges of Ni, Mn, and Sb. For the simulation we have used a lattice spacing of 0.591 nm and a Debye temperature of 270 K. A good agreement between experiments and simulation was observed for the three probed atoms. In particular, every fine-structure (high-frequency oscillations) fingerprint of a well-ordered $C1b$ structure was well reproduced in amplitude and position. To conclude, HRTEM and EXAFS studies have shown that an annealing temperature above 900 K ensured both high crystalline and chemical ordering in the prepared epitaxial NiMnSb thin films.

B. Magnetic properties

The magnetic properties of 100 nm thick (001)NiMnSb thin films grown in the optimized conditions have been studied. These magnetic properties are strongly correlated to the electronic band structure and can thus give indirect evidence of the half-metallic character. Classical hysteresis loops were measured by a SQUID. As expected, our samples possessed in-plane magnetization due to thin-film shape anisotropy. Hysteresis loops were thus measured with the field parallel to the sample plane. The obtained loops were square with a

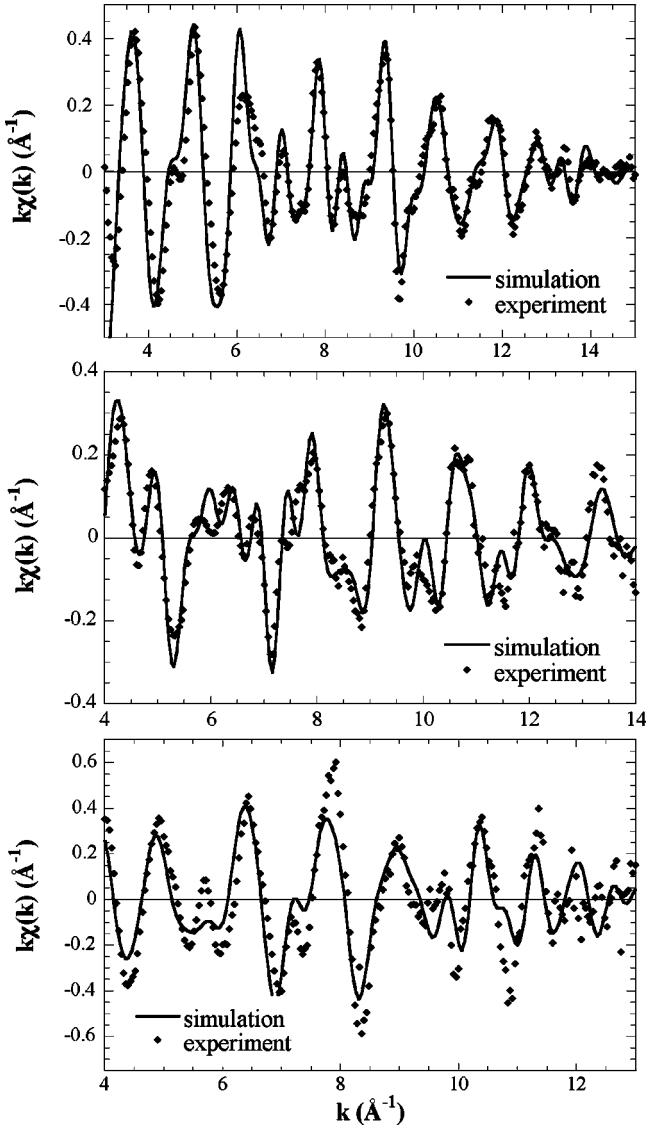

FIG. 8. Experimental EXAFS oscillations recorded at the *K* edges of Mn (top) and Ni (middle) and at the L_I edge of Sb (bottom) on a thick (001)NiMnSb film prepared in the optimized conditions. The EXAFS oscillations have been simulated by using the FEFF code. The simulation parameters are $a_{NiMnSb}=0.591$ nm and $T_{Debye}=270$ K.

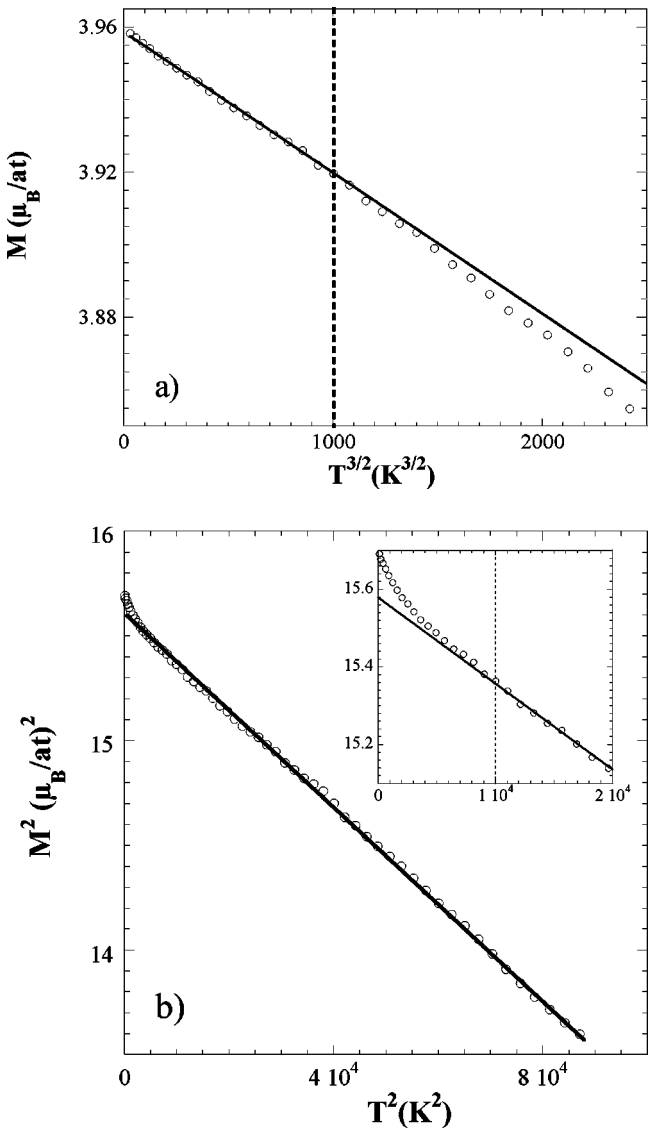

FIG. 9. Temperature dependence of the saturation magnetization of a thick NiMnSb(001) layer (a) below 100 K (left), $M \sim T^{3/2}$; and (b) above 100 K (right), $M^2 \sim T^2$. Black lines are guides for the eye.

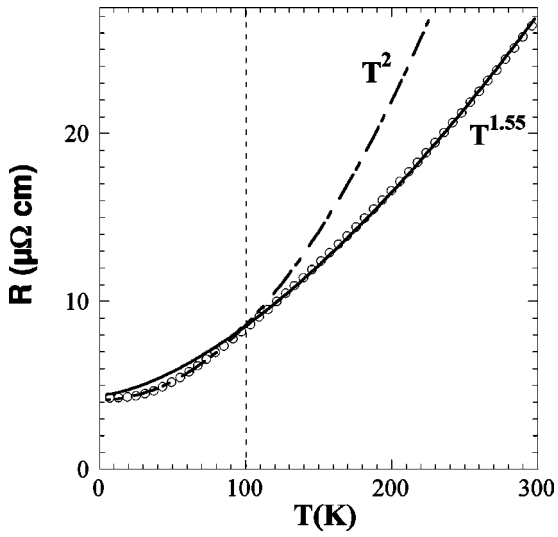

FIG. 10. Temperature dependence of the resistivity of a thick NiMnSb(001) layer and corresponding fits at low (<100 K) and high (>100 K) temperatures.

coercive field of 15 Oe and a high remanent magnetization (90%) at room temperature. The value of the coercive field presented only a few dependencies with temperature. No significant in-plane magnetocrystalline anisotropy has been detected along the main crystalline directions. The saturation magnetization was found to be equal to $3.9 \pm 0.2 \mu_B$/f.u. This value is consistent with the expected $4 \mu_B$/f.u. determined from band-structure calculations[1] and with the value measured on bulk single crystals by polarized neutron-diffraction experiments.[13]

The temperature dependence of the magnetization is reported in Fig. 9. Two different regimes could be distinguished. Below 100 K, the magnetization M varied linearly as a function of $T^{3/2}$, whereas above 100 K, M^2 varied linearly as a function of T^2. This typical behavior is identical to what has been observed in bulk NiMnSb, and also in NiMnSb thin films prepared by sputtering,[40,41] and was attributed to a transition from a low-temperature localized ferromagnetism in which collective spin-wave excitations predominate (as expected for a half-metal) to a high-temperature itinerantlike ferromagnetism in which spin fluctuations contribute to the decay of the magnetization.[40,41] Let us note that a similar $T^{3/2}$ law has also been observed in the half-metallic CrO_2 compound below 100 K.[42]

In bulk materials[43] and sputtered thin films,[44] two regimes were also observed in the temperature evolution of the resistivity, which were assumed to be the consequence of a crossover from a half-metallic to a regular metallic ferromagnetic state. A similar behavior was observed on the present NiMnSb thin films (Fig. 10). Below 100 K, the resistivity followed a T^2 variation law, while at higher temperatures a $T^{1.55}$ law was observed. This observed reduction of the resistivity below 100 K compared to the high temperature $T^{1.55}$ law was predicted by Otto *et al.*,[12] who found that due to the absence of a minority-spin density of state, spin-flip electron diffusion is not possible anymore in the half-metallic state leading to the observed resistivity decrease. Thus, at low temperature, the main contribution to the resistivity comes from the thermally excited spin waves (the phonon contribution is negligible), and the temperature dependence of the resistivity follows a quadratic law. At higher temperature, on the contrary, several diffusion processes occur and the resistivity is due to spin waves (T contributions), phonons (T contributions), and spin fluctuations ($T^{5/3}$ contributions) (Ref. 45) in the material. The value of the resulting high-temperature exponent of the resistivity ($a = 1.55$) is thus intermediate between 1 and 5/3 as experimentally observed. Similar observations are reported in Ref. 40. To conclude, bulk magnetic and transport properties of our (001)NiMnSb thin films hint at the existence of a half-metallic state at low temperature ($T < 100$ K).

We have also studied the magnetic surface properties of (001) NiMnSb epitaxial films by using the element-selective technique of x-ray magnetic circular dichroism (XMCD) on samples prepared in the MBE apparatus coupled to the

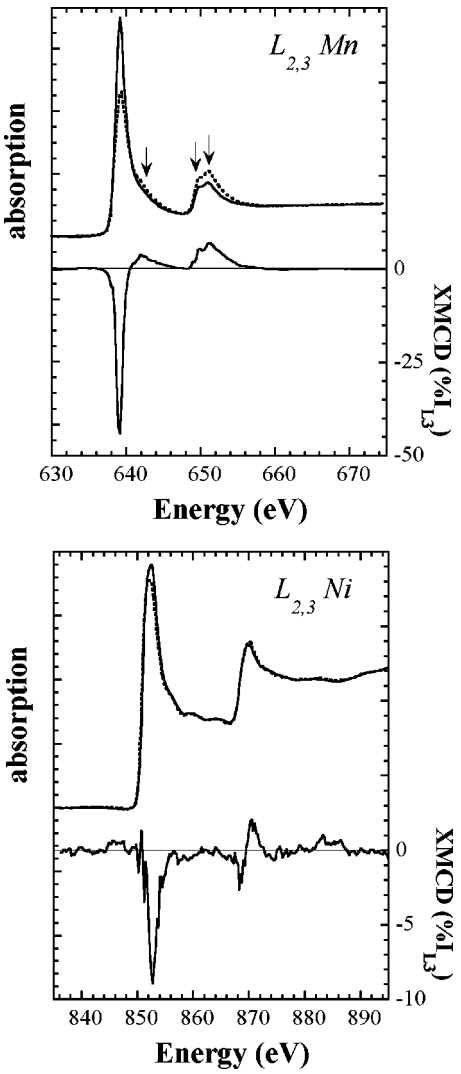

FIG. 11. X-ray-absorption spectra and XMCD signals recorded at 20 K with an applied field of ± 1 T at the $L_{2,3}$ absorption edges of Mn (top) and Ni (bottom). Multiplet structures at the Mn edge are marked by arrows.

beamline. The presented XMCD spectra are not corrected from the incident photon polarization [measured as 52% on a (001)Fe single crystal]. Figure 11 presents the absorption edges and deduced dichroism spectra recorded at 20 K with an applied field of ± 1 T and an angle of 70° between the x-ray beam and the surface normal, at the $L_{2,3}$ edges of the elements Ni and Mn. A clear dichroic signal was measured at the $L_{2,3}$ edge of Ni, corresponding to a significant magnetic moment on the Ni atoms in the NiMnSb unit cell. The application of the sum rules to this signal[46,47] gave access to a magnetic moment value of $0.2\mu_B$ per nickel atom, compared to the $0.25\mu_B$ value predicted by band-structure calculations,[1,3,48] in excellent agreement with available neutron-diffraction data.[13] On the contrary, the Mn $L_{2,3}$ absorption edge presented a huge dichroism of 43% (83% with a full circular polarization of the photon beams), with the same sign as the Ni dichroic signal.

Thus, Mn atoms presented a strong magnetic moment and a ferromagnetic coupling with Ni atoms in the crystal. It is, however, not possible to determine the absolute value of the magnetic moment on the Mn sites in the crystal since the sum rules are well known to be invalid for Mn due to the weak spin-orbit coupling, leading to a mixing of the electronic transitions at the L_3 and L_2 edges.[49]

The application of the sum rules to the Mn XMCD gave thus a underestimated value of $3\mu_B$ per Mn atom. Nevertheless, an exact value of $3.7\mu_B$ could be deduced from the knowledge of the saturation magnetization ($3.9\mu_B$) and the Ni atoms' magnetic moment ($0.2\mu_B$). Another interesting feature on the measured x-ray-absorption spectra was the general shape of the $L_{2,3}$ edge of Mn. Indeed, the absorption spectra did not present a metallic shape but exhibited a fine structure of the L_3 and L_2 edges (marked by arrows). This multiplet structure, corresponding to an ''atomic''-like behavior, has already been reported for the surface of a bulk NiMnSb sample scraped by a diamond file under vacuum[50] and can be explained by taking into account the strong hybridization between Mn $3d$ and Sb $5p$ orbitals. This hybridization has a tendency to localize the Mn electronic energy levels and thus leads to the structured absorption edges experimentally observed. It should be noted that the Mn oxidization also leads to a multiplet in the Mn L edge.[49] Consequently, one may argue that oxidization of a NiMnSb surface could not be easily identified. This is, however, not true since the two peaks observed at the Mn L_2 edge are separated by 1 eV in pure NiMnSb and by 1.7 eV in fully oxidized NiMnSb. As a consequence, experiments performed on partly oxidized NiMnSb surfaces showed three different peaks at the L_2 edge, coming from the contributions of MnO and MnSb hybridizations simultaneously. The effect of oxygen contamination is consequently easy to detect on the Mn L edge.

We have also investigated the temperature dependence of the XMCD signal at the $L_{2,3}$ absorption edge of Mn to check for an eventual change of amplitude associated to the transition from a normal ferromagnetic state through a half-metallic state at low temperature. According to the selection rules,[46,47] the disappearance of available electronic states at the Fermi level for the minority-spin direction could indeed lead to a disappearance of authorized electronic transitions during the absorption process. Figure 12 reports the evolution of the dichroism spectra recorded at the $L_{2,3}$ absorption edges of Mn versus temperature, in the range 20–200 K. The variation of the relative amplitude of the dichroic signal at the L_3 edge is also plotted in the inset. The magnetic field equal to 0.1 T was applied during the measurement and the angle between the surface normal and the x-ray beam was 45°. In these conditions, due the strong in-plane anisotropy, the magnetization is still in-plane during the measurement. With a 52% polarization, and a net XMCD signal of 83% as shown previously, the dichroic signal should be equal here to 30%. This is actually what we observe. Moreover, contrary to recent observations on NiMnSb thin films prepared by sputtering,[51] no significant evolution was observed in the investigated temperature range neither on the general shape of the absorption spectra nor on the amplitude of the dichroic signal. We only observed a small decrease of the XMCD signal with increasing temperature. This effect is not surprising and similar to the magnetization evolution with tempera-

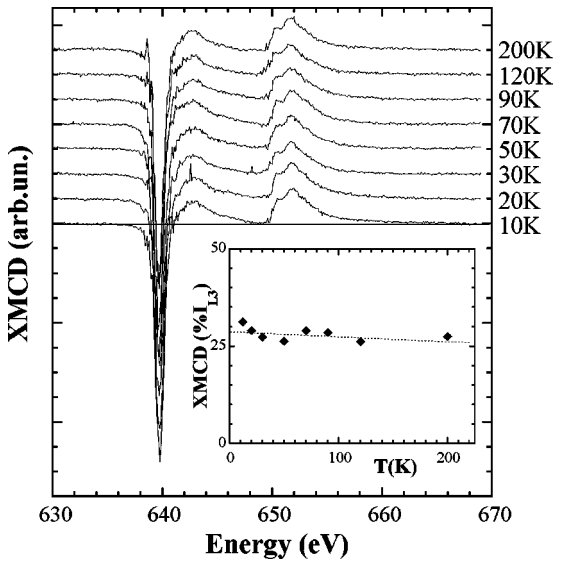

FIG. 12. Temperature dependence of the XMCD spectra and of the XMCD relative amplitude (inset) in the range 10–200 K.

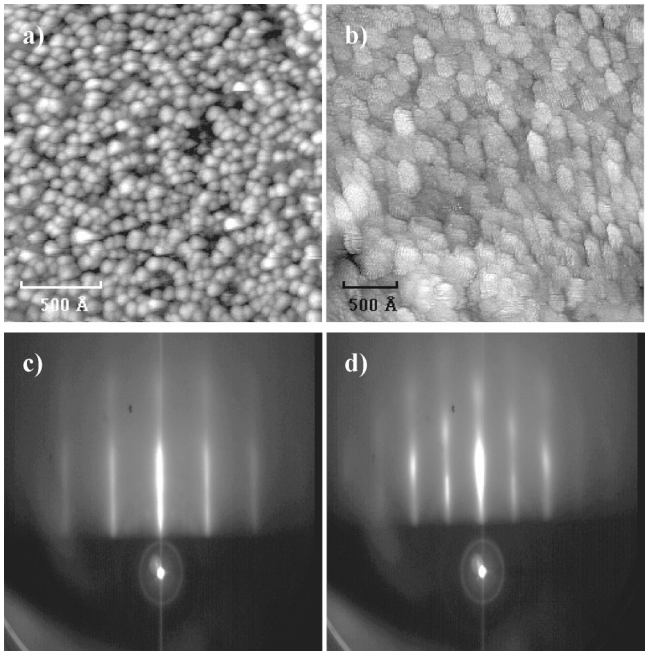

FIG. 13. STM images of a 1 nm (a) and 2.5 nm (b) thick MgO(001) layer deposited at 700 K on NiMnSb(001) and corresponding RHEED patterns in the [100] (c) and [110] (d) azimuths.

ture observed in macroscopic magnetic measurements. One should note that the dramatic increase of the XMCD signal at the $L_{2,3}$ Mn and Ni absorption edges reported in Ref. 51 below 80 K, interpreted as a huge decrease of the Mn and Ni magnetic moments associated to a bulk magnetic phase transition, is not compatible with macroscopic magnetization measurements versus temperature reported in the present paper and elsewhere.[40,41] Moreover, the main difference in Borca *et al.*'s[51] work is that our XMCD spectra are measured with an applied magnetic field, and Borca *et al.*'s work was performed at remanence. Consequently, their results may rather be explained by a strong increase of the remanent magnetization due to some drastic change in the anisotropy. We have not checked this point in detail. To conclude, our XMCD measurements have confirmed the large magnetic-moment value on the Mn atoms ferromagnetically coupled with a $0.2\mu_B$ moment on the Ni atoms, in good agreement with band-structure calculations. Nevertheless, contrary to the above-reported magnetization (Fig. 9) and transport measurements (Fig. 10) no significant singularity was observed around 100 K. Thus, our results are consistent with the fact that the assumed crossover from the low-temperature half-metallic state to a normal metallic ferromagnetic state is not associated to a magnetization redistribution on the unit crystal cell. On the other hand, one should also notice that the sample depth probed in these XMCD measurements is around 7 nm and these experiments are rather surface sensitive. We can thus conclude that the magnetic properties (moments distribution) of the NiMnSb free surface are similar to the bulk magnetic properties studied by bulk sensitive techniques such as neutron-diffraction experiments.[13]

V. NiMnSb/MgO/ NiMnSb(001) HETEROSTRUCTURES

We have integrated the previously studied high-quality NiMnSb thin films in fully epitaxial NiMnSb/insulator/NiMnSb heterostructures for the preparation of magnetic tunnel junctions. Several different candidate materials were investigated for the insulating tunnel barrier such as GaSb(001) and vanadium oxides, but the most promising results were obtained with MgO(001) as discussed hereafter. The oxide layer was grown by electron bombardment from bulk MgO.[29–31] Indeed, Vassent *et al.*[30] showed that the sublimation of MgO is congruent, even if the observed sublimated flux is essentially constituted by Mg and O atoms (not by MgO molecules). This method provides a simple way to prepare stochiometric MgO layers. We have thus studied the growth of thin MgO deposits (typically in the range 1–6 nm) on top of NiMnSb epitaxial thick layers (typically 50 nm) prepared in the optimized conditions reported in Sec. III. The crystalline quality of the obtained insulating barriers was controlled by RHEED for various substrate temperatures, from room temperature up to 950 K. For growth temperature in the range 300–700 K, the RHEED patterns analysis evidences a single-crystalline epitaxy of MgO on NiMnSb with the epitaxial relations $(001)\mathrm{MgO}\|(001)\mathrm{NiMnSb}$ and $[110]\mathrm{MgO}\|[100]\mathrm{NiMnSb}$ (Fig. 13). At 300 K, the observed RHEED patterns presented spotty diffraction rods, typical of some surface roughness of the oxide layer. This roughness had a tendency to decrease with increasing substrate temperature up to 700 K. Above this growth temperature, additional diffraction rings were superimposed to the streak patterns, indicating the presence of polycrystalline MgO areas. From these observations, the best compromise between the crystalline and morphological qualities of the MgO barrier was found for a growth temperature of 700 K. For this temperature, the MgO growth is epitaxial but presents a Volmer-Weber three-dimensional (3D) growth mode, as no RHEED intensity oscillations could be observed during deposition. This was confirmed by STM observations on a 1 nm thick

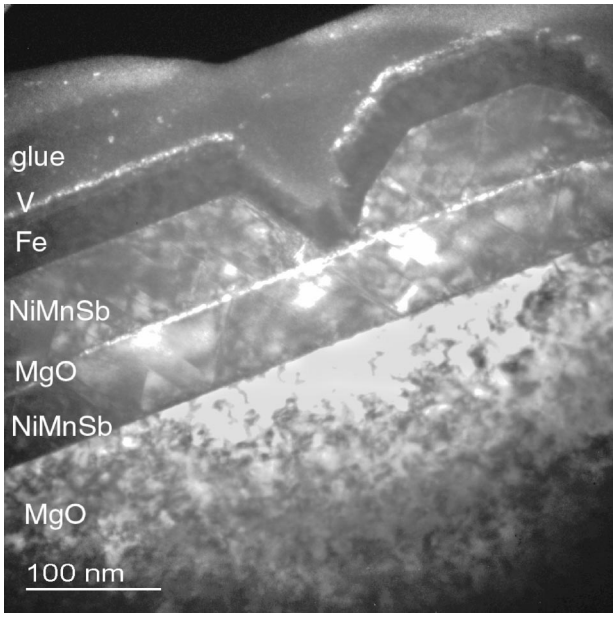

FIG. 14. TEM image of a NiMnSb(70 nm)/MgO(3 nm)/ NiMnSb(70 nm)/ Fe(20 nm) heterostructure, where the top electrode was grown at 850 K.

MgO deposit as reported in Fig. 13(a). For this thickness range, the surface morphology is made of a flat NiMnSb underlayer and 3D MgO islands with a typical height of 1.5 nm and a high nucleation density. Such 3D growth is clearly not a good feature for preparing a continuous oxide barrier. However, the percolation is observed to occur at low MgO thicknesses, as shown by AES. Indeed, the high-energy (above 400 eV) Sb, Mn, and Ni Auger peaks are no more observed when covering the surface by a 3 nm thick MgO layer. This result also means that no surface segregation of one of the Heusler alloy components occurs. Moreover, the ratio of oxygen on magnesium Auger peaks measured on this MgO barrier is similar to the same ratio measured on bulk MgO. This confirms the correct chemical stochiometry of the MgO barrier. These barrier morphological characteristics are confirmed by transmission electron microscopy (TEM) observations on NiMnSb/MgO/NiMnSb trilayers (Fig. 14 and Fig. 15). The MgO barrier is observed to be well registered on NiMnSb and is continuous over a long distance (at least longer than 0.5 μm) with a regular thickness. To conclude, despite a three-dimensional growth mode, it was possible to produce continuous epitaxial MgO(001) thin layers on NiMnSb(001) films, with a minimum thickness in the range 2–3 nm.

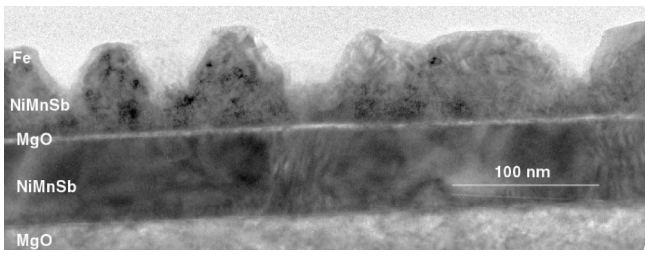

FIG. 15. TEM image of a NiMnSb(70 nm)/MgO(3 nm)/ NiMnSb(70 nm)/ Fe(20 nm) heterostructure, where the top electrode was grown at 500 K.

Since spin-dependent tunneling is very sensitive to interfacial properties of the metal-oxide junction, the magnetic properties of the NiMnSb layer close to the NiMnSb-MgO interface has to be checked and compared to those of the free surface. For this purpose, we have reproduced similar XMCD experiments at the $L_{2,3}$ Mn absorption edge, as previously reported in Sec. IV, on NiMnSb samples covered with a 7 nm thick MgO layer. Thanks to the relatively low probe depth of the x-ray-absorption experiments using the total electron yield technique, the presence of this relatively thick MgO capping layer allowed us to be very sensitive to the magnetic properties of the NiMnSb very close to the interface. For instance, similar experiments were performed on NiMnSb films covered with vanadium[27] (for spin-valve applications). Although the vanadium growth on NiMnSb is layer by layer without interdiffusion up to 900 K, strong modifications were observed on both the Mn absorption edge shape and XMCD intensity. This indicates that this capping technique is very sensitive to some modifications located at the interface. In the case of NiMnSb films covered by MgO, no change has been observed on the absorption edge spectra compared to the results reported in Fig. 11. This means that Mn is not oxidized at the NiMnSb/MgO interface. Moreover, the resulting XMCD signal has not decreased compared to the results obtained on an uncovered NiMnSb surface. Consequently, no magnetic dead layer close to the oxide barrier due to a potential oxidization of the NiMnSb surface during MgO growth was evidenced. To conclude, the produced NiMnSb/MgO bilayer is a suitable basis for preparation of NiMnSb-based magnetic tunnel junctions. However, the NiMnSb electronic properties near the Fermi level could be affected, but this method does not allow us to go further.

The next step in the junction preparation process is the growth of a second epitaxial ferromagnetic electrode on top of the insulating barrier. For this purpose, the MgO barrier is very convenient since many ferromagnetic metals or alloys [such as Fe(001), Ni(001), FeNi(001), and FeCo(001)] are well known to grow epitaxially on MgO(001). Nevertheless, we have tried to grow a second epitaxial NiMnSb electrode on top of the MgO layer in order to prepare MTJ's with two half-metallic electrodes which are the most promising heterostructures for magnetotransport applications. We have studied two types of samples, for which the 50 nm thick top NiMnSb electrode was grown as reported in Sec. III, with substrate temperatures of 850 K and 500 K, respectively. In both cases, a 20 nm thick Fe(001) layer was grown on top of the second electrode in order to increase its coercive field. Typical TEM images obtained on 850 K and 500 K second electrode grown samples are presented in Fig. 14 and Fig. 15, respectively.

Depending on the growth temperature, different morphological properties of the second NiMnSb electrode are observed due to the bad wetting of NiMnSb on the oxide layer. The low magnification micrograph in Fig. 14 is a dark field image realized by selecting the (200) MgO reflection which

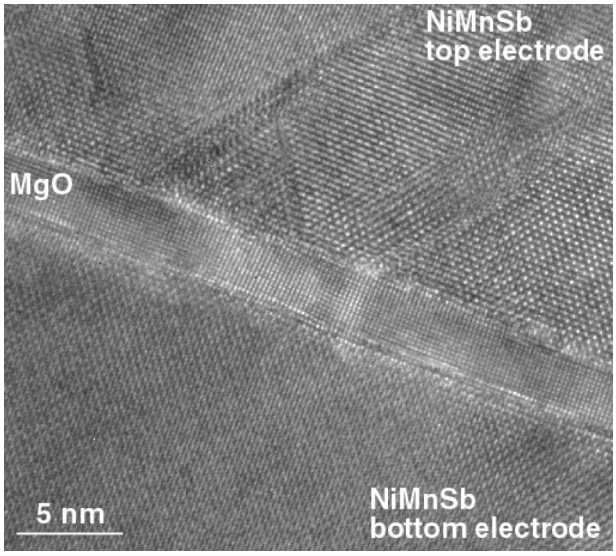

FIG. 16. HRTEM micrograph of the samples shown in Fig. 15, showing the good registry between the three layers, and the sharp interfaces.

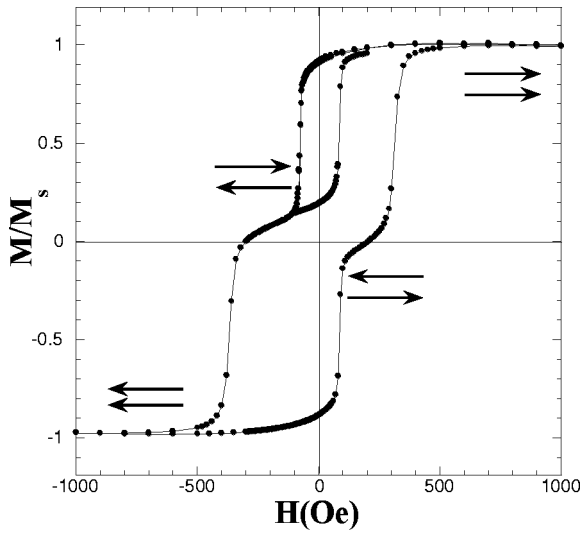

FIG. 17. Hysteresis loops measured at 5 K on the sample of Fig. 16. The magnetic field is applied in the plane of the sample.

is superposed to the (110) V one. Therefore, the bright areas correspond to the MgO and V layers. This micrograph shows the 3D growth of the upper NiMnSb layer MgO barrier. Indeed, the NiMnSb layer is not continuous and consists of large and isolated three-dimensional islands, with dominating (111) and (100) facets corresponding to dense atomic planes. This tendency to develop (111) facets has already been observed during the growth of the first NiMnSb electrode (see Sec. III). Locally, one can observe that between two isolated NiMnSb 3D islands, the Fe layer is directly in contact with the MgO barrier. These observed discontinuities are incompatible with the preparation of half-metallic magnetic tunnel junctions including half-metallic electrodes. When the top electrode is grown at a lower temperature (500 K, Fig. 15), the morphology of the top NiMnSb electrode was highly improved. The top NiMnSb layer is indeed rough, but continuous over the MgO barrier. This analysis also shows that the structural continuity of these MgO/NiMnSb interfaces is excellent as presented in the HRTEM micrograph in Fig. 16. Moreover, the top and bottom interfaces are sharp. However, stacking fault parallel to (111) planes are clearly visible. It should also be noted that the stacking faults density is decreased when the growth temperature is increased. These defects are probably due to the misfit between NiMnSb and MgO.

The hysteresis loops obtained at 5 K on this second sample are presented in Fig. 17. Two magnetization jumps are clearly observed corresponding to the separated reversal of the two NiMnSb electrodes. The magnetic configuration of the trilayer is represented along the hysteresis loop by arrows. The antiparallel alignment of the two electrodes is achieved on a large scale of field. A minor loop for which the magnetization of the only NiMnSb bottom layer (soft electrode) was switched is also presented. The coupling field between the two ferromagnetic layers through the insulating barrier is observed to be weak. To conclude, it was possible to integrate NiMnSb single-crystalline layers in fully epitaxial NiMnSb/MgO/NiMnSb heterostructures which are compatible with the preparation of magnetic tunnel junctions.

VI. CONCLUSIONS

In summary, we have demonstrated that fully epitaxial magnetic tunnel junctions including half-metallic NiMnSb electrodes may be grown by MBE. First of all, single NiMnSb layers were shown to present all the structural, chemical, magnetic, and electronic properties observed in the bulk, or in NiMnSb thin films grown by sputtering.[44,24] This is an important point since it means that the electronic properties of NiMnSb thin films are not very sensitive to the preparation technique. However, this does not hold anymore for the NiMnSb film surface. A variety of surface reconstructions are observed, which depend on the preparation and growth process. This is also a pertinent observation for theoretical investigations since all the polarization calculations of the NiMnSb (001) surface were performed assuming a bulk terminated surface. In this study $(2\times1, 3\times1, 4\times1)$ surface arrangements were observed depending on the growth temperature. However, we have not evidenced the corresponding chemical ordering which leads to these superstructures. This task needs some more specific characterization means. Despite this difficulty, we observed that the flattest surfaces compatible with MTJ's are obtained with the 4×1 reconstruction. In a second step, we demonstrated that the epitaxy of a continuous MgO single-crystalline barrier is possible on such surfaces. Another important feature is that the NiMnSb/MgO interface is ideal from the structural and chemical points of view, a crucial point for keeping the electron polarization at the interface. However, we do not yet know if the NiMnSb half-metallic behavior is preserved at the interface or in the first monolayer below the surface. To address this important point, spin-resolved x-ray photoemission spectroscopy experiments are in progress. Another test is to prepare MTJ's by using etching and lithography, in order to test their magnetoresistive behavior. This work is also in progress.

*Corresponding author. FAX: (+33)3 8391 2083. Email address: andrieu@lpm.u-nancy. fr

[1] R.A. de Groot, F.M. Müller, P.G. van Engen, and K.H.J. Buschow, Phys. Rev. Lett. **50**, 2024 (1983).
[2] E. Kulatov and I.I. Mazin, J. Phys.: Condens. Matter **2**, 343 (1990).
[3] S.J. Youn and B.I. Min, Phys. Rev. B **51**, 10 436 (1995).
[4] G. Prinz, Phys. Today **48**, 58 (1995).
[5] J.H. Park, E. Vescovo, H.J. Kim, C. Kwon, R. Ramesh, and T. Ventakesan, Nature (London) **392**, 794 (1998).
[6] K.L Kobayashi, T. Kimura, H. Saweda, K. Terakura, and Y. Tokura, Nature (London) **395**, 677 (1998).
[7] Y. Ji, G.J. Strijkers, F.Y. Yang, C.L. Chien, J.M. Byers, A. Anguelouch, Gang Xiao, and A. Gupta, Phys. Rev. Lett. **86**, 5585 (2001).
[8] P. Seneor, A. Fert, J.-L. Maurice, F. Montaigne, F. Petroff, and A. Vaurès, Appl. Phys. Lett. **74**, 4017 (1999).
[9] K. Endo, J. Phys. Soc. Jpn. **29**, 643 (1970).
[10] P.J. Webster and R.M. Mankikar, J. Magn. Magn. Mater. **42**, 300 (1984).
[11] R.B. Helmholdt, R.A. de Groot, F.M. Müller, P.G. van Engen, and K.H.J. Bushow, J. Magn. Magn. Mater. **43**, 249 (1984).
[12] M.J. Otto, H. Feil, R.A. van Woerden, J. Wijngaard, P.J. van der Valk, C.F. van Bruggen, and C. Haas, J. Magn. Magn. Mater. **70**, 33 (1987).
[13] C. Hordequin, E. Lelièvre-Berna, and J. Pierre, Physica B **234-236**, 603 (1997).
[14] K.E.H.M. Hanssen, P.E. Mijnarends, L.P.L.M. Rabou, and K.H.J. Buschow, Phys. Rev. B **42**, 1533 (1990).
[15] F.B. Mancoff, B.M. Clemens, E.J. Singley, and D.N. Basov, Phys. Rev. B **60**, R12 565 (1999).
[16] D. Orgassa, H. Fujiwara, T.C. Schulthess, and W.H. Butler, Phys. Rev. B **60**, 13 237 (1999).
[17] C.T. Tanaka, J. Nowak, and J.S. Moodera, J. Appl. Phys. **81**, 5515 (1997).
[18] C.T. Tanaka, J. Nowak, and J.S. Moodera, J. Appl. Phys. **86**, 6239 (1999).
[19] C. Hordequin, J.P. Nozières, and J. Pierre, J. Magn. Magn. Mater. **183**, 225 (1998).
[20] J.A. Caballero, A.C. Reilly, Y. Hao, J. Bass, W.P. Pratt Jr., F. Petroff, and J.R. Childress, J. Magn. Magn. Mater. **198-199**, 55 (1999).
[21] G.A. de Wijs and R.A. de Groot, Phys. Rev. B **64**, 020402(R) (2001).
[22] G.L. Bona, F. Meier, M. Taborelli, E. Bucher, and P.H. Schmidt, Solid State Commun. **56**, 391 (1985); W. Zhu, B. Sinkovic, E. Vescovo, C. Tanaka, and J.S. Moodera, Phys. Rev. B **64**, 060403(R) (2001).
[23] R.J. Soulen Jr., J.M. Byers, M.S. Osofsky, B. Nadgorny, T. Ambrose, S.F. Cheng, P.R. Broussard, C.T. Tanaka, J. Nowak, J.S. Moodera, A. Barry, and J.M.D. Coey, Science **282**, 85 (1998).
[24] D. Ristoiu, J.P. Nozières, C.N. Borca, T. Komesu, H.K. Jeong, and P.A. Dowben, Europhys. Lett. **49**, 624 (2000).
[25] D. Ristoiu, J.P. Nozières, C.N. Borca, B. Borca, and P.A. Dowben, Appl. Phys. Lett. **76**, 2349 (2000).
[26] W. Van Roy, J. De Boeck, B. Brijs, and G. Borghs, Appl. Phys. Lett. **77**, 4190 (2000).
[27] P. Turban, Ph.D. thesis, Université Henri Poincaré (Nancy I), 2001; P. Turban, S. Andrieu, E. Snoeck, B. Kierren, and C. Teodorescu, in Proceedings of the Magnetic Multilayers 2001 Conference (MML'01), Aachen, Germany, June 2001 [J. Magn. Magn. Mater. (to be published)].
[28] J.P. Schlomka, M. Tolan, and W. Press, Appl. Phys. Lett. **76**, 2005 (2000).
[29] S. Yadavalli, M.H. Yang, and C.P. Flynn, Phys. Rev. B **41**, 7961 (1990).
[30] J.L. Vassent, A. Marty, B. Gilles, and C. Chatillon, J. Cryst. Growth **219**, 434 (2000).
[31] W. Wulfhekel, M. Klaua, D. Ullmann, F. Zavaliche, J. Kirschner, R. Urban, T. Monchesky, and B. Heinrich, Appl. Phys. Lett. **78**, 509 (2001).
[32] F. Dulot, P. Turban, B. Kierren, J. Eugène, M. Alnot, and S. Andrieu, Surf. Sci. **473**, 172 (2001).
[33] P. Turban, L. Hennet, and S. Andrieu, Surf. Sci. **446**, 241 (2000).
[34] P.J. Dobson, B.A. Joyce, J.H. Neave, and J. Zhang, J. Cryst. Growth **81**, 1 (1987).
[35] D.E. Sayers, E.A. Stern, and F.W. Lytle, Phys. Rev. Lett. **27**, 1204 (1971).
[36] S.I. Zabinsky, J.J. Rehr, A. Ankudinov, R.C. Albers, and M.J. Eller, Phys. Rev. B **52**, 2995 (1995).
[37] C.T. Chen, F. Sette, Y. Ma, and S. Modesti, Phys. Rev. B **42**, 7262 (1990).
[38] H. Lee, R. Lowe-Webb, W. Yang, and P.C. Sercel, Appl. Phys. Lett. **72**, 812 (1998).
[39] M. Wojcik, W. van Roy, E. Jedryka, S. Nadolski, G. Borghs, and J. de Boeck, in Proceedings of the Magnetic Multilayers 2001 Conference (MML'O1), Aachen, Germany, June 2001 [J. Magn. Magn. Mater. (to be published)].
[40] C. Hordequin, D. Ristoiu, L. Ranno, and J. Pierre, Eur. Phys. J. B **16**, 287 (2000).
[41] D. Ristoiu, J.P. Nozières, and L. Ranno, J. Magn. Magn. Mater. **219**, 97 (2000).
[42] A. Barry, J.M.D. Coey, L. Ranno, and K. Ounadjela, J. Appl. Phys. **83**, 7166 (1998).
[43] J. Pierre, R.V. Skolozdra, J. Tobola, S. Kaprzyk, C. Hordequin, M.A. Kouacou, I. Karla, R. Currat, and E. Lelièvre-Berna, J. Alloys Compd. **262-263**, 101 (1997).
[44] C. Hordequin, J. Pierre, and R. Currat, J. Magn. Magn. Mater. **162**, 75 (1996).
[45] K. Ueda and T. Moriya, J. Phys. Soc. Jpn. **39**, 605 (1975).
[46] B.T. Thole, P. Carra, F. Sette, and G. van der Laan, Phys. Rev. Lett. **68**, 1943 (1992).
[47] P. Carra, B.T. Thole, M. Altarelli, and X. Wang, Phys. Rev. Lett. **70**, 694 (1993).
[48] I. Galanakis, S. Ostanin, M. Alouani, H. Dreyssé, and J.M. Wills, Phys. Rev. B **61**, 4093 (2000).
[49] S. Andrieu, E. Foy, H. Fischer, M. Alnot, F. Chevrier, G. Krill, and M. Piecuch, Phys. Rev. B **58**, 8210 (1998).
[50] A. Kimura, S. Suga, T. Shishidou, S. Imada, T. Muro, S.Y. Park, T. Miyahara, T. Kaneko, and T. Kanomata, Phys. Rev. B **56**, 6021 (1997).
[51] C.N. Borca, T. Komesu, H.K. Jeong, P.A. Dowben, D. Ristoiu, C. Hordequin, J.P. Nozières, J. Pierre, S. Stadler, and Y.U. Idzerda, Phys. Rev. B **64**, 052409 (2001).